University of Groningen

Bachelor Thesis

The prevalence of steam atmospheres on hot rocky exoplanets

Author:
Boyd Willem van der Plaat *(S3736113)*

Supervisors:
dr. Tim Lichtenberg
dr. Robert J. Graham
Second Examinor:
dr. Harish Vedantham

June 29, 2023

Abstract

The composition of the atmospheres found on Earth and Earth-like exoplanets primarily arises from the exchange processes occurring between their interiors and atmospheres during their hot rocky phase. Such planets are predominantly composed of magma oceans in their early phase of evolution. The gases present in the atmosphere during this hot rocky state play a significant role in determining its future composition. Thus, comprehending the specific elements required and their respective abundances for the formation of Earth-like atmospheres is crucial for identifying and characterizing exoplanets that have the potential to become habitable. Furthermore, this understanding can provide valuable insights into the early stages of our own planet. Currently, there is ongoing debate regarding the prevalence of steam in these types of environments. Therefore, the research question I have investigated revolves around assessing the influence of steam on various aspects of the developing atmosphere. To accomplish this, I conducted an analysis to investigate the potential impacts of different water abundances on components such as vertical temperature structures, molar compositions of atmospheres, emission spectra, and total spectral flux. The results of my study indicate that steam abundance has an impact on all of these components, except for the total spectral flux. Here, the observed behavior in the total spectral flux plots deviated from the expected patterns. The results show a non-dependence on water abundance which changes at higher surface temperatures. These results imply an inconsistency between previous research result and the behaviour produced by the used numerical code. Hence, future analyses may improve upon this aspect by locating the source of the inconsistency. The outcomes of this analysis provide valuable insights into the prevalence of steam in the atmospheres of hot rocky exoplanets. This knowledge expands our understanding of the formation and evolution of these atmospheres, shedding light on the conditions necessary for the development of habitable environments.

1 Introduction

Early Earth or Earth-like planets contain certain volatile elements which are the main components stimulating the prospective formation of an atmosphere of such celestial bodies. The volatile elements most likely to have an influence on the atmospheres of planets like Earth are hydrogen, carbon, nitrogen, and oxygen (Lichtenberg et al., 2022). While the young planet is predominantly in a molten state, the volatile composition of the atmosphere exerts great influence on the subsequent planetary evolution. The molten oceans exchange and transport the volatile elements between the molten interior and the atmosphere. This dictates the future atmospheric compositions, which plays a vital role in determining its habitability of planets. Considerable uncertainties persist regarding the composition and prevailing dominance of elements in these young atmospheres that result in the formation of an atmosphere similar to that of the Earth's. Upcoming surveys are expected to provide more insight and comprehensive data pertaining to these exoplanets (Apai et al. (2019), Gaudi et al. (2020), Meixner et al. (2019), Quanz et al. (2021), The-LUVOIR-Team (2019)).

Models relating to atmospheric structures can effectively analyse the data obtained from future surveys which facilitate the identification and characterization of the exoplanets in question. Currently, the models have the capability to investigate atmospheres comprising both single and multiple species. More specifically, the species considered in this analysis include H_2O, H_2, CO_2 and CO. The selection of these specific species for investigation is based on their ability to act as highly efficient absorbing agents within the unique conditions found in these juvenile planetary environments (Lichtenberg et al., 2021). Each individual species is chosen based on its unique properties and characteristics. H_2O, being a potent contributor to the greenhouse effect, has been consistently considered in the analysis of magma ocean atmospheres due to its contributing factor (Matsui & Abe (1986), Abe & Matsui (1986)). Another crucial component is H_2, which can have long-term impacts on the atmosphere through collision-induced absorption. This phenomenon arises from the inelastic collisions occurring among gas molecules (Koll & Cronin (2019), Pierrehumbert & Gaidos (2011), Zahnle et al. (1988)). Just as H_2 and H_2O, CO_2 acts as a significant greenhouse gas and plays a crucial role in shaping the composition of the atmosphere. CO_2 also has an impact on the rate of water loss in the atmosphere by affecting the cold trap temperature. The cold trap effectively removes water vapour from the surrounding atmosphere by trapping it in a condensed phase. It

controls the water escaping to space and as the temperature of the cold trap increases, the more water is lost to space (Wordsworth & Pierrehumbert, 2013). Both CO_2 and CO relate their dominance in an atmosphere due to their corresponding oxidization, which is evident in Figure 1. In this figure, their respective molar concentration is plotted against the mantle melt fraction for different oxidization states.

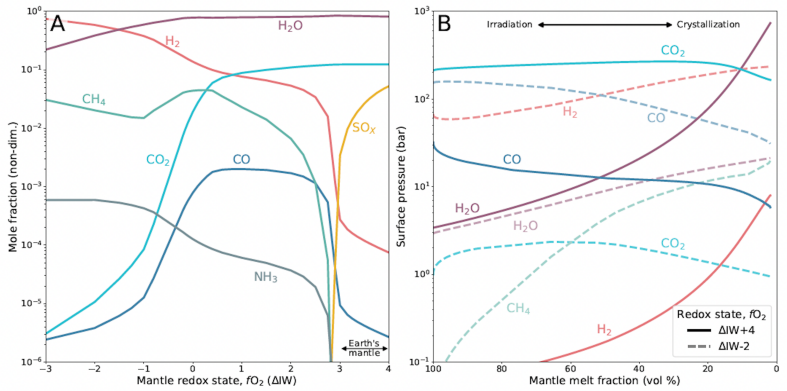

Figure 1: Simulation of outgassing of atmospheric volatiles (Lichtenberg & Miguel, 2023).

In Subplot (A), the simulation focuses on the outgassing of atmospheric volatiles from a solid planetary mantle while varying the iron-wüstite buffer. This buffer represents compounds that control oxygen fugacity as a function of temperature. On the other hand, Subplot (B) simulates a crystallizing mantle with variations in melt fraction and the iron-wüstite buffer. These plots illustrate the transition of the abundance of the primary atmospheric compounds, showcasing the shift from reduced to oxidized atmospheres in relation to oxygen fugacity. Figure 1 underscores the importance of carbon volatile species and their particular states in these atmospheres. During planet formation and magma ocean cooling, the major phase and partitioning behavior of carbon volatile species remain inadequately constrained, representing another noteworthy attribute (Lichtenberg et al., 2021).

Currently, the previously discussed models are subject to an ongoing debate. One of the aspects discussed in these debates is the role of steam in such atmospheres. While currently, N2 is the dominant species in Earth's atmosphere, water vapour is thought to dominate the atmospheric formation of these early magma ocean planets (Boukrouche et al. (2021), Lichtenberg

et al. (2021), Wordsworth & Pierrehumbert (2013)). Despite the prevailing understanding, recent petrological experiments have been interpreted to suggest that in such high-temperature atmospheric conditions, the compositions of atmospheres of Earth-like planets will be dominated by CO/CO_2 (Sossi et al., 2023). This would have a direct effect on the current characterization of Earth-like exoplanets, necessitating the need for adjustments in the observational analyses conducted by the James Web Space Telescope (JWST) and upcoming direct imaging missions.

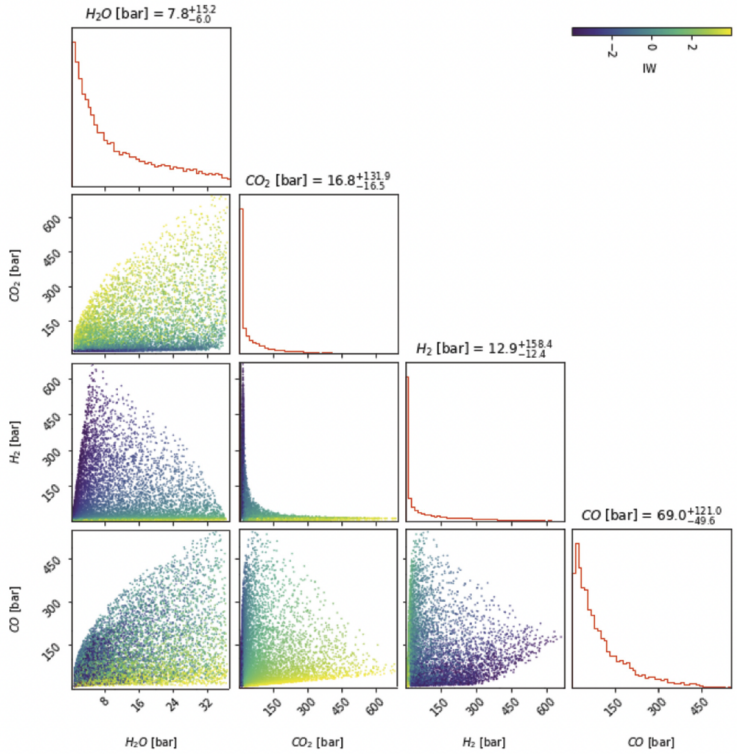

Figure 2: Corner plot of partial pressures of the four gas species present in the atmosphere of planets with a fully molten mantle, surface temperature of 2173 k, and 1 Earth mass. (Sossi et al., 2023).

Figure 2, produced by Sossi et al. (2023) illustrates the key factors considered in their suggestion. This plot was generated by the variation of three parameters (C/H, ocean masses of H, and oxygen fugacity). Each data point in the plot is colour-coded based on its corresponding oxygen fugacity value, relative to the iron-wüstite buffer, seen in the colourbar.

The authors arrive at their suggestion by demonstrating that the oxygen fugacity at the interface between the atmosphere and the magma, the C/H ratio, and the number of magma oceans on the planet collectively influence the likelihood of steam atmospheres forming on these particular types of exoplanets. Utilizing a Monte-Carlo simulation, they show that H_2O with a high solubility, relative to the other background gasses, limits the extent of its atmospheric outgassing. Based on this observation, the authors conclude that steam atmospheres are a rare occurrence on these types of exoplanets with magma oceans.

An aspect that was neglected in the Monte-Carlo simulations of these petrological experiments (Sossi et al., 2023) was the vertical temperature structure of the atmosphere. This is a crucial point, as the vertical temperature structure of the atmosphere is a primary determinant of the evolution of planetary surfaces and climates (Graham et al., 2021). I therefore used the bulk atmospheric compositions provided in Sossi et al. (2023) and ran them through a more comprehensive and sophisticated coupled model of atmospheric interaction on magma ocean planets (Graham et al., 2021). The resulting data will provide a more realistic picture of magma ocean atmospheres, granting new insights into the role of steam in early planetary evolution.

2 Methods

To understand the results produced by certain inputs into the sophisticated atmospheric coupled model, I'll first go through how the model operates. The model is a pseudoadiabat with multiple condensing components, which includes condensate retention. This assumption was not made by Lichtenberg et al. (2021), as they simulate an atmosphere with complete condensate retention. Nevertheless, there might be a lack of realism in that assumption, which needs further exploration. Because of this, Graham et al. (2021) varies the condensate retention when modeling the atmospheres of exoplanets. Taking such variables into account, Equation 1 was derived through the development of the lapse rate or multi-component pseudoadiabat equation (Graham et al., 2021).

$$\frac{d\ln T}{d\ln P} = \frac{x_d + \Sigma_i x_{v,i}}{x_d \frac{c_d x_d + \Sigma_i (x_{v,i}(c_{v,i} - R\beta_i + R\beta_i^2) + \alpha_i x_{c,i} c_{c,i})}{R(x_d + \Sigma_i \beta_i x_{v,i})} + \Sigma_i \beta_i x_{v,i}} \tag{1}$$

Equation 1 represents the lapse rate, indicating the temperature T in relation to the total pressure P. On the right side of the equation, we have x_d which represents the mole fraction of a dry gas or mixture component. The subsequent parameter, $\Sigma_i x_{v,i}$ represents the sum of individual condensable vapour components. Followed in the denominator by c_d which represents the molar specific heat at constant pressure, with units [J /K /mol], of a dry gas/mixture. Furthermore, we have $c_{v,i}$ denoting the condensing gas, and $c_{c,i}$ representing the condensate. Next is R, corresponding to the universal ideal gas constant (8.314 J/K/mol) and β_i being equal to $\frac{L}{RT}$, with L [J/mol] being the latent heat of the individual condensable components. Finally, α_i is the individual vertical component of the condensate that is retained instead of rained out. For this analysis I set the condensation at $\alpha_i = 0$, causing no condensation to be found in the atmosphere. By manipulating the lapse rate, it becomes possible to differentiate between dry and moist convection. In the case of unsaturated conditions (dry adiabat/convection), we assume an atmospheric column composed entirely of non-condensable gas. To yield an equation for the dry convection, the following assumptions were made: $\Sigma_i x_{v,i} = \Sigma_i x_{c,i} = 0$ and $x_d = 1$. When these assumptions are incorporated into Equation 1, it results in the formation of Equation 2, which represents the lapse rate for the dry adiabat.

$$\frac{d \ln T}{d \ln P} = \frac{R}{c_d} \tag{2}$$

Similarly, by assigning $x_d = 0$ and $\Sigma_i \alpha_i x_{c,i} = 0$, we can establish an equation for the moist convection, representing an atmosphere composed of condensing species that undergo instantaneous rainout. These lead to the formulation of Equation 3.

$$\frac{d \ln T}{d \ln P} = \frac{1}{\Sigma_i \beta_i x_{v,i}} \tag{3}$$

The lapse rate is a multi component equation that can also be simplified to represent a singular species. In this analysis, I will examine both the individual and multi-component solutions to derive a conclusion regarding the prevalence of steam in the atmospheres of hot rocky exoplanets. The atmospheric radiative transfer code used to implement all of these equations is known as Socrates (Edwards & Slingo, 1996). The code can be accessed by following the steps outlined on the GitHub platform (https://github.com/FormingWorlds/AEOLUS), which serves as an online collaborative coding platform. The simulations generated from the multi-component model will be executed using the individual values for the background gasses obtained from Sossi et al. (2023), seen in Figure 2. This is

done in order to evaluate their findings regarding the predominance of steam. To further investigate whether steam is a dominant factor in the formation of an Earth-like atmosphere, I analyse various distinct conditions. Most importantly, I will vary the abundance of steam in the modelled atmospheres to assess its influence on related variables.

The generation of my results will commence with the plotting of the pseudoadiabat for four distinct partial pressures. The varying partial pressures signify the absence and increasing presence of steam. By varying this input, we can gain a deeper understanding of the role of steam under specific surface temperature conditions. Subsequently, I will plot the partial pressures of steam against surface temperature at various total pressures, as well as molar concentration against surface temperature. Expanding upon these plots, a 2D representation will be generated in order to illustrate the relationship between partial pressure, surface temperature, and molar concentration at three different total pressures.

An intriguing aspect that will provide further insights into the impact of steam is its spectral influence. The spectral influence is governed by Equation 4, which states that the total upward and downward flux is the combined result of thermal and stellar components (Lichtenberg et al., 2021).

$$F_{net}^{\uparrow\downarrow} = F_{th}^{\uparrow\downarrow} + F_{*}^{\downarrow} \tag{4}$$

Equation 4 can be further derived into another equation, enabling us to conduct a comprehensive analysis relating to this study (Equation 5).

$$F_{atm}^{\uparrow} = F_{net}^{\uparrow} - F_{net}^{\downarrow} \tag{5}$$

By utilizing this equation, we can obtain the emission spectra at various different steam abundances and surface temperatures, while keeping the background gasses constant. The analysis of the spectra would reveal the specific regions in the spectra where water exerts its influence, consequently affecting the flux exiting the atmosphere. The specific regions of interest investigated relating to this analysis are commonly referred to as "water vapour windows". Within these wavelength ranges, water exhibits decreased opacity, enabling greater flux to escape in a single species atmosphere consisting of steam. This becomes more evident as I examine Figure 3.

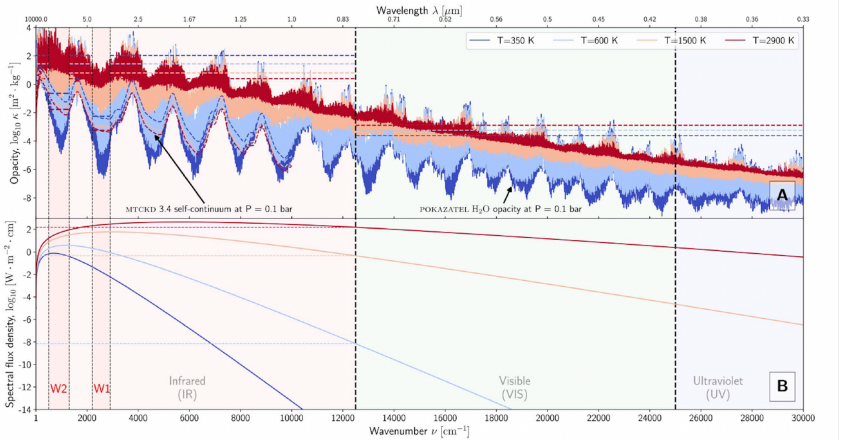

Figure 3: Plotting wavenumber and wavelength against opacity and spectral flux density (Boukrouche et al., 2021).

Figure 3 shows the opacity coefficient of water vapour between 1 and 30,000 cm^{-1}, at 0.1 total atmospheric pressure. This opacity coefficient is then plotted for four distinct surface temperatures, 350, 600, 1500, and 2900 kelvin. The solid lines represent the water vapour data from the POKAZATEL line list for selected temperatures (Tennyson et al., 2020), which is the opacity data of these regions. The dashed coloured lines indicate the self-broadened continuum plus the MT_CKD 3.4 data lines. MT_CKD is a water vapour continuum absorption model, and for these lines it ranges between 1 and 10,000 cm^{-1}. The lines corresponding to the mean opacity are the horizontal dashed lines.

In Figure 3, the two exemplary water vapour windows are denoted as W1 and W2, with the distinct colours representing various surface temperatures. Within these specific wavelength ranges, there is a notable drop in opacity, resulting in increased transmission of radiation. By systematically varying the water abundance, I can investigate the impact of these water vapour windows on my multi-species spectra at different surface temperatures. This is done because the flux of outgoing radiation into space is a primary determinant of the climate and thermal evolution of planets, which will aid in reaching a conclusion regarding the significance of water in these early atmospheres.

3 Results

The code referenced in the methods section was employed to generate the following plots. As mentioned earlier, the input values utilised were obtained from Sossi et al. (2023), seen in Figure 2, ensuring a precise comparison between their findings and mine. The surface temperature extracted from this figure was 2173 kelvin. The species considered for this analysis comprised CO, H_2, CO_2 and H_2O, with their respective partial pressures set at 69.0 bar, 12.9 bar, 16.8 bar and a variable component for steam.

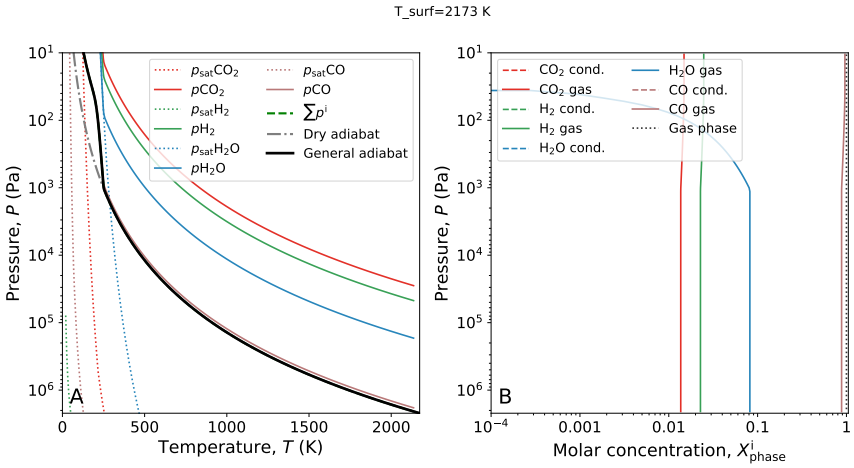

Figure 4: General adiabat plots at Surface Temperature 2173 K with individual components: H_2O at 1.8 bar (lower limit of partial pressure). Left plot depicts Pressure vs Temperature, while the right plot illustrates Pressure vs Molar Concentration.

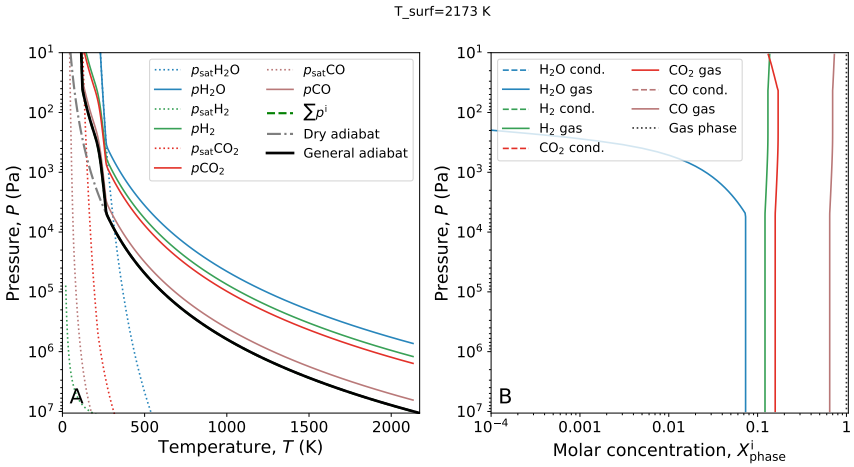

Figure 5: The same axis as in Figure 4 including general adiabat plots with Average Steam Partial Pressure (7.8 bar).

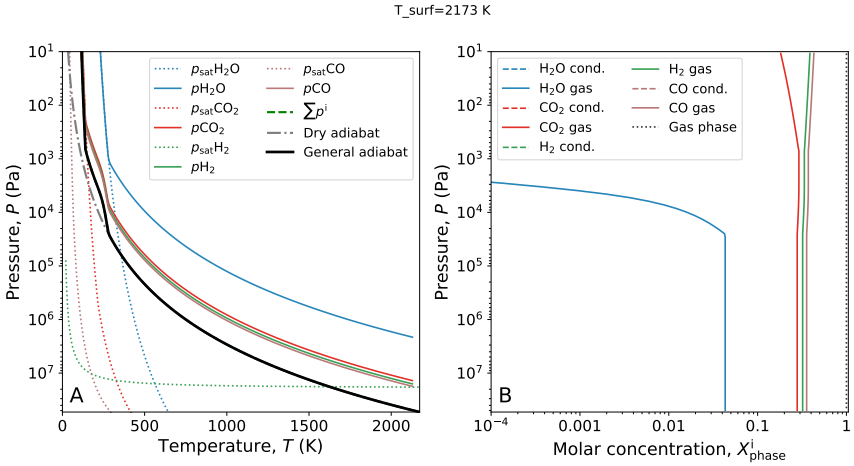

Figure 6: The same axis as in Figure 4 including general adiabat plots with Steam at Upper Limit (23.0 bar).

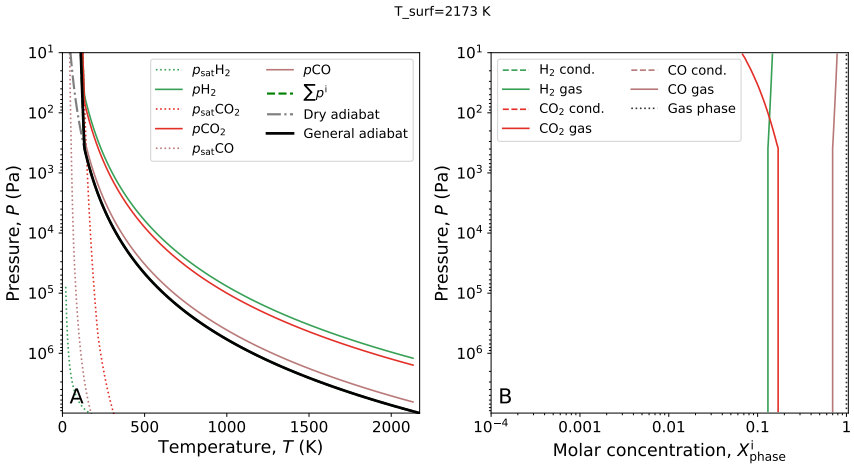

Figure 7: The same axis as in Figure 4 including general adiabat plots with Absence of Steam in the Atmosphere (0 bar).

Figures 4-7 depict the vertical temperature structure and molar compositions of atmospheres with varying steam content. The left-hand plot displays the relationship between atmospheric pressure (vertical axis) and temperature (horizontal axis). The plots depict the dry adiabat (Equation 2), which represents the thermodynamic behavior of the atmosphere until it intersects with the saturation vapour curves represented by the dashed lines. From this point onwards, the lapse rate follows the profile of moist convection (Equation 3). This characteristic applies consistently to all individual volatiles plotted, as denoted by their respective colours in the plots. An observable trend in the pseudoadiabat, as the water abundance is increased, is the reduced adherence to the dry adiabatic profile. As the partial pressure of water is increased, the adiabats of the individual background gasses gradually become overshadowed by water's influence, to the extent that they appear to follow a similar path. In the case of moist volatiles, the interaction between their saturation curve and adiabat occurs at lower pressures, excluding water.

On the right subplot in each figure, the vertical axis represents atmospheric pressure, while the horizontal axis represents molar concentration. The lines in the plot represent the individual species in their respective gas phases. The dashed lines present in the legend but not in the subplots, indicate the previously mentioned α_i set at zero, not allowing for condensate to stay in the atmosphere. The molar concentration of steam exhibits a decrease at low

atmospheric pressures. As the abundance of water increases, this decrease occurs at higher atmospheric pressures. Additionally, at high atmospheric pressures, the molar concentration of steam has a lower value when the water abundance increases. The abundance of water also influences the molar concentration of other volatiles. Specifically, the molar concentration of H_2 and CO_2 increases, while the molar concentration of CO decreases, as the partial pressure of water increases.

The next two plots build upon the previous four figures, providing further analysis and insights. The two plots depict water's partial pressure and molar concentration at three different total atmospheric pressures as a function of the surface temperature. In these figures, water's surface partial pressure is held at 7.8 bars (the average value from Sossi et al. (2023)) and surface temperature is varied from 500 to 3000 kelvin.

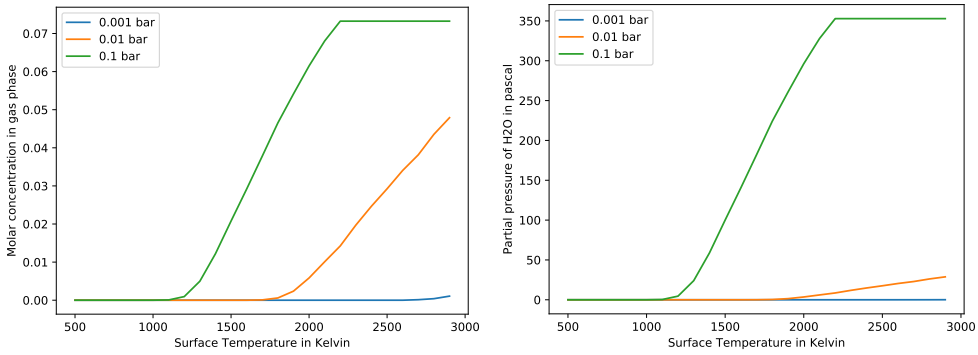

(a) (b)

Figure 8: (a) Plotting Molar concentration of steam in the atmosphere against the surface temperature in kelvin for specific partial pressures of the background gasses. (b) Plotting partial pressure of water in pascal against the surface temperature in kelvin for specific partial pressures. Plotted for three different total pressures in bar (see legend).

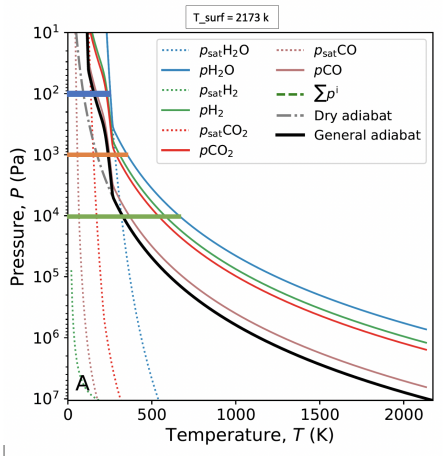

Figure 9: The left subplot in figure 5, evaluating the three atmospheric total pressures. 0.1 bar (green), 0.01 bar (orange), and 0.001 bar (blue).

Figure 9 serves as a complementary aid for comprehending the information presented in Figure 8. It illustrates the atmospheric pressures at which the simulation in Figure 8 is evaluated. The colours of the horizontal lines in Figure 9 correspond to a specific atmospheric total pressure assigned with the same colours in Figure 8. By following the lines depicted in Figure 9, one can visually trace the path until it intersects with the atmospheric partial pressure of water. This intersection represents a singular data point corresponding to a specific surface temperature (2173 K). Subsequently, in Figure 8, I examine this particular data point across a range of surface temperatures, thereby expanding our analysis beyond a single instance.

The subplots in Figure 8 demonstrate notable observations regarding the behavior of water under different atmospheric pressures and surface temperatures. At higher atmospheric pressures, both the molar concentration and partial pressure of water exhibit a steeper increase as the surface temperature rises. However, for an atmospheric pressure of 0.1 bar, there is a threshold around 2000 kelvin where the molar concentration and partial pressure of water reach a saturation point, stabilizing at approximately 0.07 and 350 pascal, respectively. In the left plot, it is evident that at lower atmospheric pressures, the molar concentration of water experiences a more gradual decrease compared to the more pronounced decline in partial pressure depicted in the right plot.

The next set of plots consists of three 2D plots corresponding to the previously mentioned atmospheric pressures. Each subplot illustrates the variation of the molar concentration of steam as a function of surface temperature and surface partial pressure of H_2O, with the three panels displaying values from the same three atmospheric pressures as in Figure 8. The range of surface partial pressure spans from the earlier used lower limit to the upper limit in pascal, while the surface temperature is ranged between 500 and 3500 in kelvin. These plots provide insights into how the abundance of water in these atmospheres influences the molar concentration of steam at different surface temperatures and atmospheric pressures.

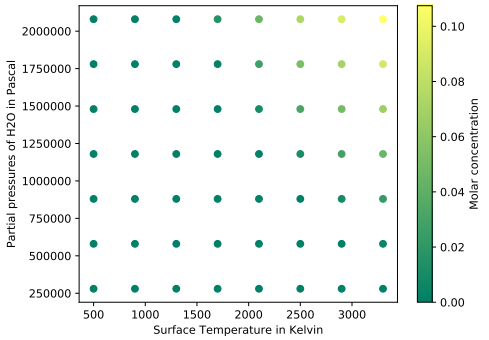

(a) Total pressure: 0.001 bar

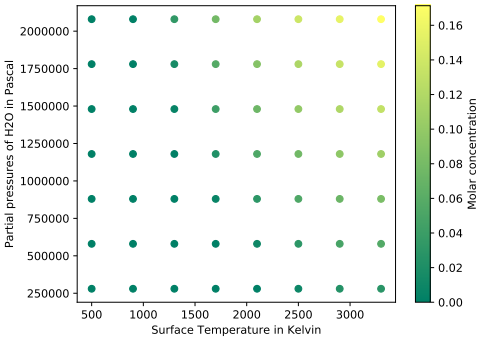

(b) Total pressure: 0.01 bar

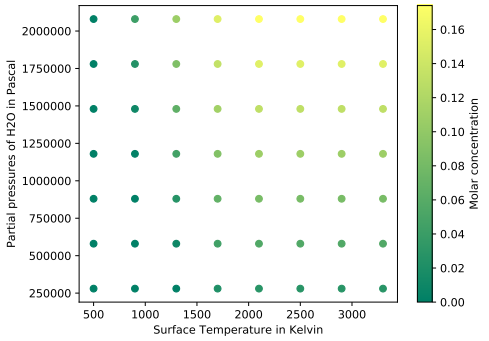

(c) Total pressure: 0.1 bar

Figure 10: A 2D plot performed at total pressure (a) 0.001 bar, (b) 0.01 bar, (c) 0.1 bar. Plotting partial pressures of water in pascal against the surface temperature in kelvin against the molar concentration of steam.

The figures reveal that as the surface temperature and partial pressure of water increase, the molar concentration of water throughout the atmosphere

also increases. Furthermore, it is worth noting that the rate of increase in molar concentration becomes more pronounced with higher atmospheric pressures. This observation becomes evident when comparing Figure 10c with Figures 10a and 10b. Additionally, at extremely low surface temperatures, the molar concentration remains consistently low across all three plots.

The subsequent plots depict the emission spectra emitted by these planetary types, considering various surface temperatures and different abundances of water. The emitted spectral flux is derived from Equations 4 and 5, which capture the radiative transfer processes. The first set of plots showcases the spectra at different surface temperatures. Additionally, two specific spectral ranges, where water exhibits influence on the spectra, are examined in greater detail through close-up plots.

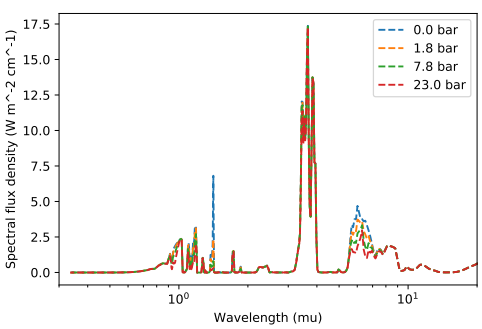

(a) Surface temperature: 1500 kelvin

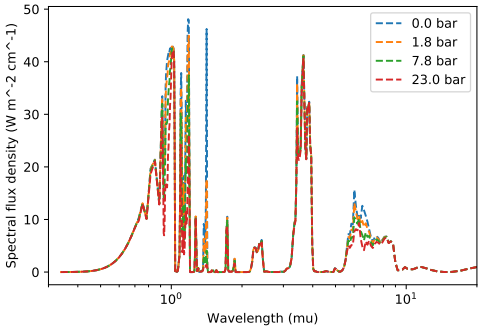

(b) Surface temperature: 2173 kelvin

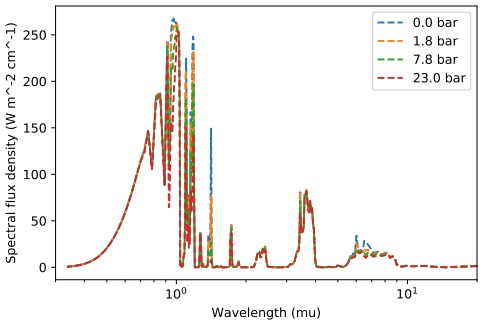

(c) Surface temperature: 3000 kelvin

Figure 11: The plot illustrates the spectral flux density in watts per square meter per centimeter as a function of wavelength in microns at different surface temperatures: (a) 1500 kelvin, (b) 2173 kelvin, and (c) 3000 kelvin. The plot shows the impact of four different partial pressures of water (as indicated in the legend) on the emitted spectra.

The spectra also exhibits variations at different water abundances within specific wavelength ranges. Notable changes in the spectra can be observed within the ranges of 0.8 - 1.05 µm, 1.075 - 1.2 µm, 1.3 - 1.5 µm, 3.3 - 3.6 µm, and 5 - 8 µm. The extent of these changes, whether an increase or decrease, is influenced by the surface temperature. At many wavelengths in these spectra, water doesn't have an effect on the emission flux. It is important to note that in many parts of the spectra, water does not significantly affect the emission flux, indicating that other factors or species dominate the radiative processes in those regions.

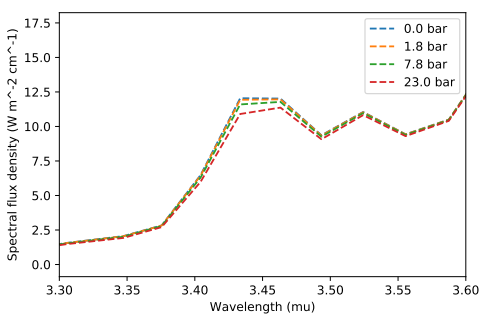

(a) Surface temperature: 1500 kelvin

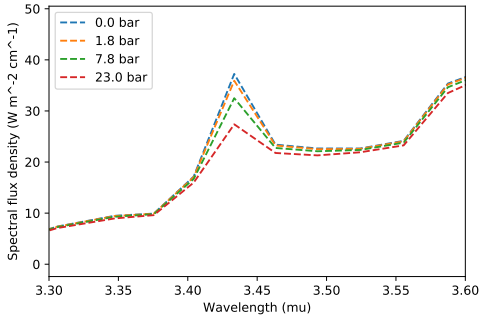

(b) Surface temperature: 2173 kelvin

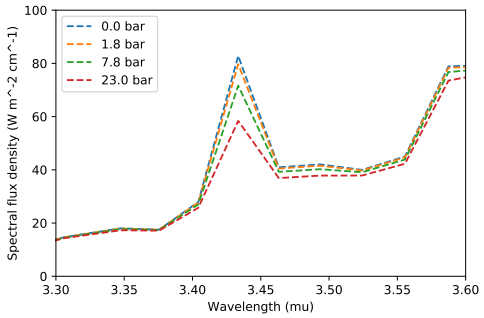

(c) Surface temperature: 3000 kelvin

Figure 12: The plots (a), (b), and (c) display the spectra within the wavelength range of 3.3 µm to 3.6 µm for different surface temperatures: (a) 1500 kelvin, (b) 2173 kelvin, and (c) 3000 kelvin.

The range examined in these plots is derived from Figure 3, more specifically W1 (water vapour window 1). The presence of a dip in opacity within this range indicates intriguing behavior. Notably, the influence of water within these specific wavelength ranges exhibits a strong dependence on the surface temperature. As the surface temperature increases, the differences in spectral flux between different water abundances become more pronounced.

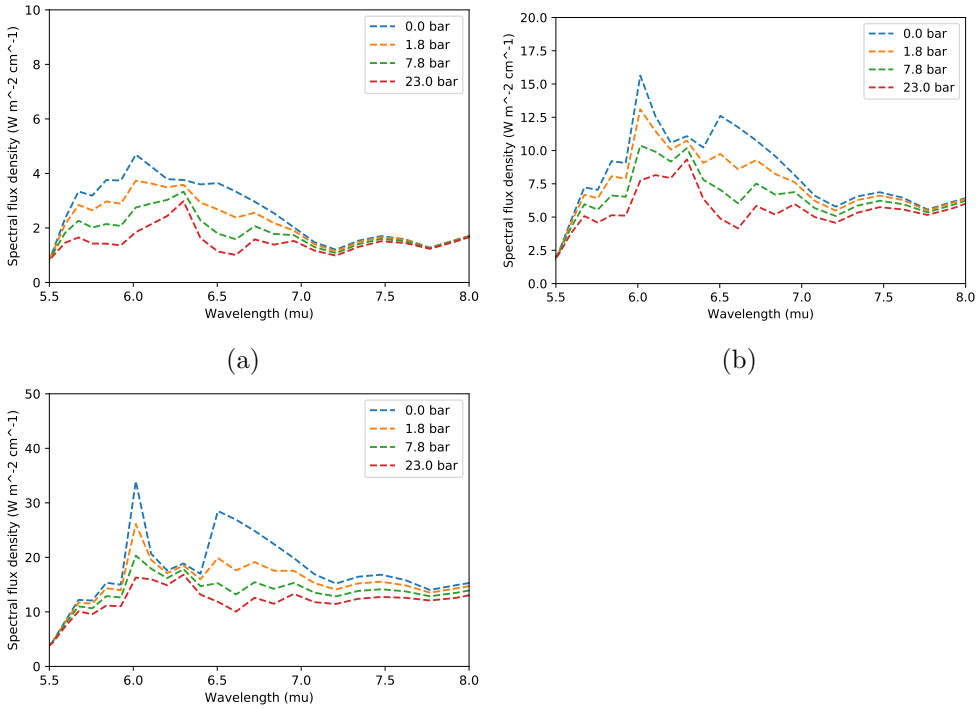

Figure 13: The plots (a), (b), and (c) display the spectra within the wavelength range of 5.5 µm to 8.0 µm for different surface temperatures: (a) 1500 kelvin, (b) 2173 kelvin, and (c) 3000 kelvin.

The range examined in Figure 13 could potentially be derived from Figure 3, although there is some uncertainty due to the scaling of Figure 3. The specific wavelength range W2 (water vapour window 2) encompasses a wide range of wavelengths. It is worth noting that as the surface temperature increases, the relative differences in spectral flux between various water abundances exhibit a relatively consistent pattern, with one notable exception. There are distinct spikes observed around 6 µm and 6.6 µm wavelengths, which introduce variations in the spectral flux.

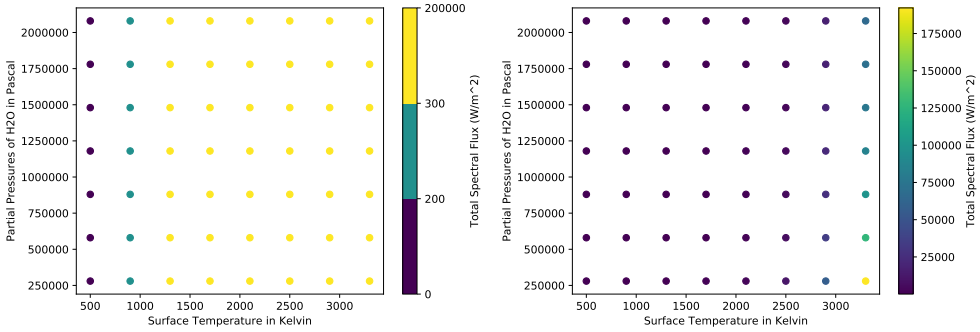

(a) (b)

Figure 14: (a) and (b) represent the same 2D plot depicting the relationship between the partial pressure of water and the surface temperature, along with the corresponding total flux density. (a) provides a colour bar indicating the specified ranges, ranging from 0 to 200, 200 to 300, and 300 to 200,000 W/m^2. (b) illustrates the total flux value for each corresponding data point.

Figure 14b illustrates that significant differences in the total flux are observed only at extreme surface temperatures. Specifically, it is evident that the total flux tends to be higher for lower partial pressures of water. On the other hand, Figure 14a presents a more focused view of the same plot, highlighting specific ranges of values within the total flux. This plot exhibits a preference for values exceeding 300 W/m^2, indicating a tendency towards higher flux levels in the depicted data.

4 Discussion

The research question under investigation pertains to the prevalence of steam in the atmospheres of hot rocky exoplanets, considering various conditions while keeping the background gas components and their corresponding partial pressures constant. Figures 4 to 7 present the same general adiabat while varying the abundance of water. The pressure axis can be interpreted as atmospheric height, where higher values represent lower atmospheric heights. The analysis demonstrates that with increasing partial pressure of water, the adherence to the dry adiabatic profile becomes progressively shorter (Equation 2). The dry adiabat represents the atmospheric profile comprised of a

completely non-condensable gas. In the analysed graphs, it is observed that as we move higher in the atmosphere, the general adiabat deviates from the dry adiabatic profile and starts to resemble the moist convective profile. The moist convective profile assumes instantaneous rainout conditions, where condensed water vapour precipitates out rapidly. This transition in the atmospheric behavior at higher altitudes suggests the influence of moisture and the onset of moist convection in shaping the atmospheric dynamics. The pseudoadiabat tends to deviate from the dry adiabatic profile and starts to follow the moist adiabatic profile more closely. This is because water vapour, being a condensable component, affects the thermodynamic behavior of the atmosphere. As the water abundance increases in the atmosphere, it enhances the likelihood of condensation and precipitation processes (Graham et al., 2021). As it increases, the relative abundance compared to its background gasses gets bigger, which supports the pseudoadiabats following of the moist convection profile for longer. The graphs showcasing the individual species and their adiabats demonstrate the progressive dominance of water as the partial pressure of steam increases.

The right-hand side plots in Figures 4 to 7 depict the vertical variation of molar concentration within the atmosphere and continues the trend of examining different water abundances at the earlier mentioned background gas compositions. The condensation lines were not plotted in these figures, due to the condensation retention being set at 0. However, the abundance of the gas component was. As previously discussed, steam condenses at lower atmospheric temperatures, which is the reason why the molar concentration of water drops off to zero at certain heights. The higher the abundance of water is, the lower in the atmosphere it condenses. This observation aligns with the findings depicted in the left-hand plots, where the extension of the moist convective profile is observed to be more pronounced with increasing water abundance. The condensation height of steam decreases with its increase of abundance. As you increase the abundance of steam, it can reach saturation at higher temperatures. The changes in molar concentrations of the background species can be attributed to the chemical reactions and equilibria involving steam and the background gasses.

To gain a comprehensive understanding of the behavior of steam under different circumstances, I also varied the abundance of other components in the system. In Figure 8a and 8b I explore the influence of surface temperature for three different total pressures. To provide visual aid and facilitate comparison, I created Figure 9, which was generated using the data from

the left-hand plot in Figure 5. The three differently coloured lines in Figure 9 correspond to the three distinct colours representing the total pressures in Figure 8. In Figure 9 the surface temperature is fixed at 2173 kelvin, which provides a single data point in Figure 8. For this figure, I examine a range of values for the surface temperature. This way I can examine the three atmospheric heights and their corresponding molar concentrations (8a) and partial pressures of steam (8b). Additionally, the background gasses are set at their constant average value, entailing that the surface pressure of water is at 7.8 bar. At lower atmospheric heights it is shown that both the molar concentration, as well as the partial pressure increase faster as the surface temperature increases. Steam condenses at lower atmospheric pressures, which is visible at 0.001 bar, where the molar concentration of steam barely increases. This happens because, as the pressure decreases, the temperature required to maintain steam in a gaseous state also decreases. Only if the surface temperature were to reach unrealistic values, the molar concentration of steam would increase at such heights. There are also visible cut off points for both 7a and 7b, happening at around 0.07 molar concentration and 350 pascal partial pressure of steam. Both of these maximum values are only reached in lower atmospheric heights at higher surface temperatures. This is due to the vertical nature of the temperature. At low altitudes and high surface temperatures, steam can't condense, reaching maximum values for its partial pressure in the atmosphere and molar concentration. These plots show the importance of surface temperature for different atmospheric heights.

In Figure 10, I introduce variations in another component to gain insights into the behavior of steam in these atmospheres. Figure 10 displays plots with varying partial pressures of steam, along with the same range of surface temperatures observed in the previously discussed plots. The 2D plots in Figure 10 examine the molar concentration of steam at specific quantities, revealing that as atmospheric height decreases, the molar concentration of steam tends to increase. These plots demonstrate the influence of both water abundance and surface temperature on the molar concentration of steam. As the water abundance increases, the molar concentration of steam increases as well. However, at low surface temperatures and low partial pressures, the molar concentration exhibits minimal variation. These findings underscore the significant role played by water abundance and surface temperature in shaping the molar concentration of steam.

The spectra presented in Figure 11 provide compelling evidence for the influ-

ence of steam on the outgoing flux. The outgoing flux is the key determinant of the evolution of the planetary surface since it determines the net cooling rate (Lichtenberg et al., 2021). As seen in the presented figures, the presence of water has an impact on flux leaving the atmosphere, which is composed of both background gasses and varying water abundance values. The analysis of the spectra reveals both differences and notable similarities across the range of the water abundances. Regions where water appears to have a negligible influence on the spectra can be attributed to the dominant opacity contributions from the background species. The rationale behind these spectral differences can be elucidated by referring to Figure 3 in the methods section. The analysis of the windows presented in Figure 3 offers valuable insights into the observed variations in the emission spectra. The specific spectral windows highlighted in my analysis range from 3.3 to 3.6 µm and from 5 to 8 µm, as seen in Figure 12 and 13. Figure 3 provides a clear depiction of a significant window in the spectral range of 2.5 to 5 µm, where the opacity of water exhibits a noticeable decrease. This significant drop can explain the behavior of the plots in Figure 12. The water dropping in opacity allows for the spectra to change with the abundance of water. This spectral change becomes more pronounced as surface temperature increases. This is due to the enhanced excitation of molecules and increased energy levels. These higher energy levels lead to more active molecular transitions, resulting in more significant alterations in the emission spectra. This results in a relationship between the surface temperature, the spectral changes, and the importance of water on the outgoing flux at higher surface temperatures. Figure 13, representing the spectral window between 5 - 8 µm, can be further explained using the plot in Figure 15 (Bertie & Lan, 1996).

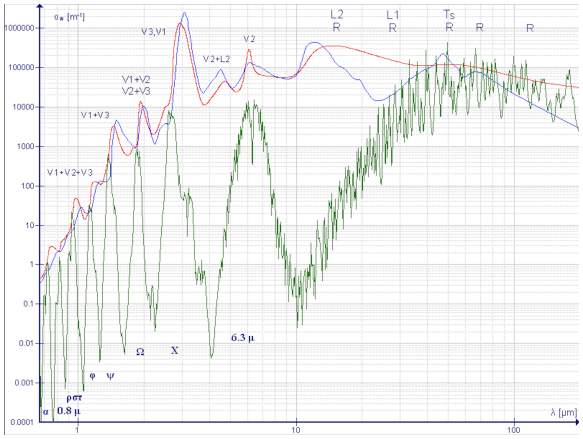

Figure 15: Absorption coefficient for water - liquid (red line), vapour (green) and ice (blue).

The prominent vapour line depicted in green at 6.3 µm in the graph plays a crucial role in understanding the observed differences in flux. Similar to Figure 3, the presence of the dip in this vapour line indicates a specific range where water vapour exhibits significant opacity. Figure 13 is influenced by the surface temperature in the same way as Figure 12. In Figure 13 it is shown that at certain wavelengths water abundance provides bigger flux differences than at others. This is due to the specific absorption and emission features of both water and the background gasses. Expanding on these plots, I examine Figure 14, in which we can observe the overall trends and variations in the total spectral flux as the abundance of water is varied. This allows us to assess the impact of water on the overall emission spectrum and understand how it contributes to the overall radiative properties of the system. This plot relates directly to Figure 16 (Lichtenberg & Miguel, 2023).

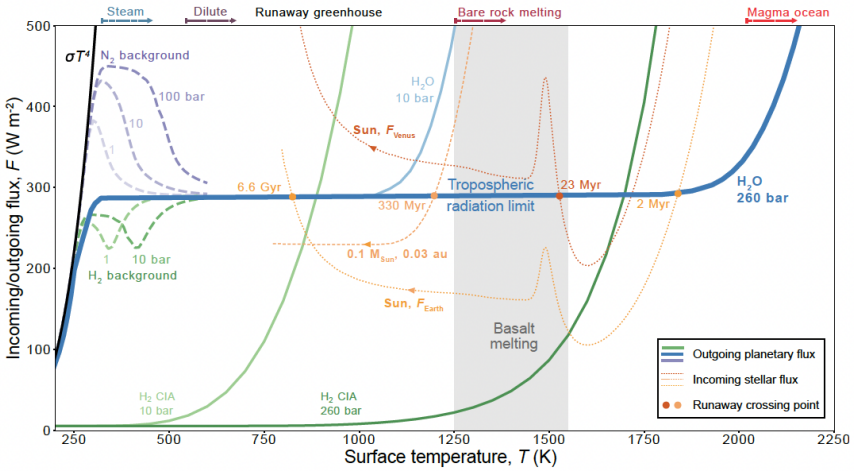

Figure 16: Competition of outgoing planetary and incoming stellar radiation for various types of atmospheres as a function of surface temperature (Lichtenberg & Miguel, 2023).

In Figure 16, a notable trend can be observed across different water abundances. Specifically, there is a consistent plateau or level-off point in the spectral flux density at approximately 280 W/m^2 across a wide range of surface temperatures. It shows the spectral flux significantly increases at higher surface temperatures, particularly for higher water abundances. For comparison with the plots in Figure 14, at 100000 pascal we should see a trend at which the total flux stays around 280 W/m^2 until just after 1000 kelvin where it shoots up. As seen in Figure 14b, at around 100000 pascal, it stays relatively low until it reaches unrealistic surface temperatures. This behavior is inconsistent with what should seen. Nevertheless, my results show little dependence on steam in the atmosphere, when it actually should be following the expected trends. The differences in the model used for Figure 14 and Figure 16 suggests an underlying difference in the simulation software which needs further investigated in the future.

5 Conclusion

This thesis aims to investigate the prevalence of steam atmospheres on hot rocky exoplanets, addressing a topic that holds significance in the ongoing debate surrounding volatiles and their dominance in early Earth-like atmospheres. A previous study proposed the dominance of CO_2/CO over steam

in these atmospheres (Sossi et al., 2023). To examine the validity of this claim, I conducted an analysis that replicated their approach while incorporating the vertical component of the atmosphere and varying the abundance of steam. Resolving this debate would contribute to future surveys and direct imaging efforts focused on characterizing and identifying such exoplanets, as well as providing insights into the early stages of Earth.

To answer the research question, I examined multiple components of atmospheric structures. Figures 4-7 provided initial indications of the importance of water abundance at different atmospheric heights. Figure 8 further evaluated this phenomenon by demonstrating the strong dependence of molar concentration and atmospheric partial pressure of water on the vertical temperature component. This suggests that the overlooked aspect in Sossi et al. (2023) actually plays a crucial role in atmospheric evolution.

The outgoing flux of an atmosphere is crucial in its evolution, and Figures 11, 12, and 13 revealed that water abundance has a significant impact on spectral flux density at various wavelength regions. However, a limitation in this research emerged due to a malfunction in the model used to generate Figure 14. Consequently, the plots in Figure 14 indicate that the partial pressure of water does not influence the total flux. This discrepancy becomes apparent when comparing the results to those presented in Figure 16, which demonstrate the expected behavior of water abundance on the total flux. This misalignment between the generated results and the model for Figure 16 suggests a disparity between the currently used simulation software and the model utilized for Figure 16. Further investigation is necessary to address this discrepancy and delve deeper into the underlying differences in the simulation software. Future work would greatly benefit from addressing these limitations and conducting further investigations could enhance our understanding of steam atmospheres on hot rocky exoplanets.

References

Abe, Y., & Matsui, T. (1986). Early evolution of the earth: Accretion, atmosphere formation, and thermal history. *Journal of Geophysical Research: Solid Earth*, *91*(B13), E291-E302. Retrieved from https://agupubs.onlinelibrary.wiley.com/doi/abs/10.1029/JB091iB13p0E291 doi: https://doi.org/10.1029/JB091iB13p0E291

Apai, D., Milster, T. D., Kim, D. W., Bixel, A., Schneider, G., Liang, R., & Arenberg, J. (2019, jul). A thousand earths: A very large aperture, ultralight space telescope array for atmospheric biosignature surveys. *The Astronomical Journal*, *158*(2), 83. Retrieved from https://dx.doi.org/10.3847/1538-3881/ab2631 doi: 10.3847/1538-3881/ab2631

Bertie, J. E., & Lan, Z. (1996, Aug). Infrared intensities of liquids xx: The intensity of the oh stretching band of liquid water revisited, and the best current values of the optical constants of h2o(l) at 25°c between 15,000 and 1 cm-1. *Appl. Spectrosc.*, *50*(8), 1047–1057. Retrieved from https://opg.optica.org/as/abstract.cfm?URI=as-50-8-1047

Boukrouche, R., Lichtenberg, T., & Pierrehumbert, R. T. (2021, oct). Beyond runaway: Initiation of the post-runaway greenhouse state on rocky exoplanets. *The Astrophysical Journal*, *919*(2), 130. Retrieved from https://doi.org/10.3847%2F1538-4357%2Fac1345 doi: 10.3847/1538-4357/ac1345

Edwards, J. M., & Slingo, A. (1996, April). Studies with a flexible new radiation code. I: Choosing a configuration for a large-scale model. *Quarterly Journal of the Royal Meteorological Society*, *122*(531), 689-719. doi: 10.1002/qj.49712253107

Gaudi, B. S., Seager, S., Mennesson, B., Kiessling, A., Warfield, K., Cahoy, K., ... Zellem, R. (2020). *The habitable exoplanet observatory (habex) mission concept study final report.*

Graham, R. J., Lichtenberg, T., Boukrouche, R., & Pierrehumbert, R. T. (2021, oct). A multispecies pseudoadiabat for simulating condensable-rich exoplanet atmospheres. *The Planetary Science Journal*, *2*(5), 207. Retrieved from https://dx.doi.org/10.3847/PSJ/ac214c doi: 10.3847/PSJ/ac214c

Koll, D. D. B., & Cronin, T. W. (2019, aug). Hot hydrogen climates near the inner edge of the habitable zone. *The Astrophysical Journal*, *881*(2), 120. Retrieved from https://dx.doi.org/10.3847/1538-4357/ab30c4 doi: 10.3847/1538-4357/ab30c4

Lichtenberg, T., Bower, D. J., Hammond, M., Boukrouche, R., Sanan, P., Tsai, S.-M., & Pierrehumbert, R. T. (2021). Vertically resolved magma ocean–protoatmosphere evolution: H2, h2o, co2, ch4, co, o2, and n2 as primary absorbers. *Journal of Geophysical Research: Planets*, *126*(2), e2020JE006711. Retrieved from https://agupubs.onlinelibrary.wiley.com/doi/abs/10.1029/2020JE006711 (e2020JE006711 2020JE006711) doi: https://doi.org/10.1029/2020JE006711

Lichtenberg, T., & Miguel, Y. (2023). Super-earths and earth-like exoplanets. *Treatise on Geochemistry*.

Lichtenberg, T., Schaefer, L. K., Nakajima, M., & Fischer, R. A. (2022). *Geophysical evolution during rocky planet formation.*

Matsui, T., & Abe, Y. (1986). Evolution of an impact-induced atmosphere and magma ocean on the accreting earth. *Nature*, *319*(6051), 303–305.

Meixner, M., Cooray, A., Leisawitz, D., Staguhn, J., Armus, L., Battersby, C., ... Webster, C. (2019). *Origins space telescope mission concept study report.*

Pierrehumbert, R., & Gaidos, E. (2011, may). Hydrogen greenhouse planets beyond the habitable zone. *The Astrophysical Journal Letters*, *734*(1), L13. Retrieved from https://dx.doi.org/10.1088/2041-8205/734/1/L13 doi: 10.1088/2041-8205/734/1/L13

Quanz, S., Absil, O., Benz, W., Bonfils, X., Berger, J.-P., Defrère, D., ... Wyatt, M. (2021, 09). Atmospheric characterization of terrestrial exoplanets in the mid-infrared: biosignatures, habitability, and diversity. *Experimental Astronomy*, *54*. doi: 10.1007/s10686-021-09791-z

Sossi, P. A., Tollan, P. M., Badro, J., & Bower, D. J. (2023). Solubility of water in peridotite liquids and the prevalence of steam atmospheres on rocky planets. *Earth and Planetary Science Letters*, *601*, 117894. Retrieved from

https://www.sciencedirect.com/science/article/pii/S0012821X22005301 doi: https://doi.org/10.1016/j.epsl.2022.117894

Tennyson, J., Yurchenko, S. N., Al-Refaie, A. F., Clark, V. H. J., Chubb, K. L., Conway, E. K., ... Yurchenko, O. P. (2020, November). The 2020 release of the ExoMol database: Molecular line lists for exoplanet and other hot atmospheres. , *255*, 107228. doi: 10.1016/j.jqsrt.2020.107228

The-LUVOIR-Team. (2019). The luvoir mission concept study final report, arxiv eprints, arxiv :1912.06219.

Wordsworth, R. D., & Pierrehumbert, R. T. (2013, nov). Water loss from terrestrial planets with co2-rich atmospheres. *The Astrophysical Journal*, *778*(2), 154. Retrieved from https://dx.doi.org/10.1088/0004-637X/778/2/154 doi: 10.1088/0004-637X/778/2/154

Zahnle, K. J., Kasting, J. F., & Pollack, J. B. (1988). Evolution of a steam atmosphere during earth's accretion. *Icarus*, *74*(1), 62-97. Retrieved from https://www.sciencedirect.com/science/article/pii/0019103588900310 doi: https://doi.org/10.1016/0019-1035(88)90031-0